JOURNAL OF GEOPHYSICAL RESEARCH, VOL. 105, NO. D16, PAGES 20,757–20,772, AUGUST 27, 2000

Use of a GCM to explore sampling issues in connection with satellite remote sensing of the Earth radiation budget

Laura D. Fowler,[1] Bruce A. Wielicki,[2] David A. Randall,[1] Mark D. Branson,[1] Gary G. Gibson,[2] and Fredrick M. Denn[3]

Abstract. Collocated in time and space, top-of-the-atmosphere measurements of the Earth radiation budget (ERB) and cloudiness from passive scanning radiometers, and lidar- and radar-in-space measurements of multilayered cloud systems, are the required combination to improve our understanding of the role of clouds and radiation in climate. Experiments to fly multiple satellites "in formation" to measure simultaneously the radiative and optical properties of overlapping cloud systems are being designed. Because satellites carrying ERB experiments and satellites carrying lidars- or radars-in space have different orbital characteristics, the number of simultaneous measurements of radiation and clouds is reduced relative to the number of measurements made by each satellite independently. Monthly averaged coincident observations of radiation and cloudiness are biased when compared against more frequently sampled observations due, in particular, to the undersampling of their diurnal cycle. Using the Colorado State University General Circulation Model (CSU GCM), the goal of this study is to measure the impact of using simultaneous observations from the Earth Observing System (EOS) platform and companion satellites flying lidars or radars on monthly averaged diagnostics of longwave radiation, cloudiness, and its cloud optical properties. To do so, the hourly varying geographical distributions of coincident locations between the afternoon EOS (EOS-PM) orbit and the orbit of the ICESAT satellite set to fly at the altitude of 600 km, and between the EOS PM orbit and the orbits of the PICASSO satellite proposed to fly at the altitudes of 485 km (PICA485) or 705 km (PICA705), are simulated in the CSU GCM for a 60-month time period starting at the idealistic July 1, 2001, launch date. Monthly averaged diagnostics of the top-of-the-atmosphere, atmospheric, and surface longwave radiation budgets and clouds accumulated over grid boxes corresponding to satellite overpasses are compared against monthly averaged diagnostics obtained from hourly samplings over the entire globe. Results show that differences between irregularly (satellite) and regularly (true) sampled diagnostics of the longwave net radiative budgets are the greatest at the surface and the smallest in the atmosphere and at the top-of-the-atmosphere, under both cloud-free and cloudy conditions. In contrast, differences between the satellite and the true diagnostics of the longwave cloud radiative forcings are the largest in the atmosphere and at the top-of-the atmosphere, and the smallest at the surface. A poorer diurnal sampling of the surface temperature in the satellite simulations relative to the true simulation contributes a major part to sampling biases in the longwave net radiative budgets, while a poorer diurnal sampling of cloudiness and its optical properties directly affects diagnostics of the longwave cloud radiative forcings. A factor of 8 difference in the number of satellite overpasses between PICA705 and PICA485 and ICESAT leads to a systematic factor of 3 difference in the spatial standard deviations of all radiative and cloudiness diagnostics.

1. Introduction

Unscrambling the role of clouds and radiation in the climate system is a daunting task, from either a modeling or an observational standpoint. From the observational point of view, we desire a large ensemble of observations of all types of cloud systems over the globe, in all seasons. Since clouds change rapidly in space and time, we desire near-simultaneous observations of atmospheric state variables, cloud physical properties, cloud optical properties, and radiative fluxes [e.g., *Wielicki et al.*, 1995]. One of the major steps forward in this direction will be taken by the Earth Observing System (EOS) PM platform, a Sun-synchronous 1330 LT orbiting satellite planned for launch in December 2000. EOS PM will include (1) a greatly improved cloud imager for cloud physical and optical properties, MODIS (Moderate-Resolution Imaging Spectroradiometer) [*King et al.*, 1992] and (2) a greatly improved broadband Earth Radiation Budget (ERB) radiometer, CERES (Clouds and Earth Radiant Energy System) [*Wielicki et al.*, 1996].

[1]Department of Atmospheric Science, Colorado State University, Fort Collins.
[2]Atmospheric Science Division, NASA Langley Research Center, Hampton, Virginia.
[3]Analytical Services & Materials Inc., Hampton, Virginia.

Paper number 2000JD900239.
0148-0227/00/2000JD900239$09.00

EOS-PM instruments are not well suited to measure multilayered clouds, cloud base altitude, or the vertical profile of aerosol and optically very thin cloud layers. Multilayered clouds are a particular challenge to our understanding of the effect of clouds on surface longwave fluxes where the base altitude of the lowest cloud level is critical. To overcome these shortcomings, NASA has selected for launch two satellites to fly in formation with EOS PM starting in early 2003. PIC ASSO-CENA (Pathfinder Instruments for Cloud and Aerosol Spaceborne Observations-Climatologie Etendue des Nuages et des Aerosols) [*Winker and Wielicki*, 2000] is a joint French and U.S. satellite mission to add a nadir-viewing cloud and aerosol vertically profiling lidar, an oxygen A-band spectrometer, and a simple visible/infrared imager instrument to fly in formation with EOS PM. This mission intends to add vertical profile information for all aerosols and for thin to moderately thick clouds. Because the thickest clouds attenuate the lidar, the CloudSat [*Stephens*, 1998] satellite will add a 94-GHz nadir-pointing cloud radar to complement the lidar and provide cloud layering for moderate to thick cloud layers. The combination of lidar and radar is also expected to help improve the accuracy of estimates of cloud ice water path and microphysics. Because clouds change rapidly in space and time, the PIC-ASSO and CloudSat missions are planned to fly within ±6 min of the EOS-PM spacecraft at all times.

In an ideal world the active lidar and radar data on the PICASSO-CENA and CloudSat satellites, like the passive instruments on EOS PM, would scan across the satellite swath to provide a full three-dimensional view of the cloud fields. In addition, we would fly these active instruments in formation with not only EOS PM at 1330 LT but also EOS AM at 1030 LT and the Tropical Rainfall Measuring Mission (TRMM) [*Simpson et al.*, 1988] in a precessing variable local time orbit so that we could sample the diurnal cycle 6 times per day [*Young et al.*, 1998].

Power, mass, and cost limitations dictate that such observations be available in one orbit, and only at nadir in this initial mission. Because radar and lidar-active signals decrease at the square of the satellite altitude, there is clearly an advantage in placing these satellites at as low an orbit altitude as possible. The TRMM precipitation radar is the primary reason for the TRMM satellite orbit altitude of 350 km. Higher altitudes are less of a problem for passive radiometers, however, and global coverage favors higher altitudes such as the 705 km altitude of the EOS-PM platform. A second complication arises when it is desirable to formation fly multiple satellites. The period of a satellite orbit depends on altitude. As a result, two satellites with different orbit altitudes will come in and out of phase within the orbit plane, even if both satellites are in 1330 LT Sun-synchronous orbits. In summary, there are three sampling issues that will arise in matching the new lidar and radar satellite data to more traditional passive scanning radiometers: (1) the effect of satellite altitude on the fraction of the data which is nearly simultaneous in time, (2) nadir sampling versus the ~2000-km swath coverage of the passive radiometers, (3) diurnal sampling at only 1330 and 0130 LT.

The first two of these sampling issues will lead to random errors with no bias error. The last sampling issue will lead primarily to bias errors, depending on the amplitude of the diurnal cycle.

What is a reasonable time simultaneity requirement to match cloud and aerosol data from multiple spacecraft flying in formation? Experience with spatial variability of clouds on scales from 30 m to 300 km indicates that the greatest challenge will be matching lidar and radar cloud layering information rigorously to the cloud optical properties and radiative fluxes estimated by MODIS [*Baum et al.*, 2000a, b] and CERES [*Wielicki et al.*, 1996]. The time simultaneity requirements for broadband radiation and cloud optical properties (e.g., CERES and MODIS) has been specified as a range of plus or minus 6 min. This range allows matching of the cloud reflectance or cloud optical depth to a relative 1σ noise of less than 10% over a typical CERES 20 km field of view [*Wielicki et al.*, 1995].

Current technology and resource limitations restrict us to consider nadir-pointing cloud lidars and radars only. Because lidars and radars are active systems, their power requirements scale linearly with the number of fields of view, so scanning lidars and radars require much greater power or antennas to reach the same signal to noise level as passive instruments. Nevertheless, so little information is available concerning multiple cloud layer situations (estimated to be more than half of all cloud observations according to surface observers [*Warren et al.*, 1985; *Tian and Curry*, 1989; *Wang and Rossow*, 1995] that even nadir-only lidars and radars will help greatly.

For diurnal sampling, measurements 6 times per day, from either three spaced Sun-synchronous orbits or two Sun-synchronous orbits and one rapidly precessing orbit like that of the Earth Radiation Budget Satellite (ERBS) [*Barkstrom and Smith*, 1986], have been shown to be adequate for the diurnal sampling of shortwave and longwave radiative fluxes and cloud optical properties. As a reference, the International Satellite Cloud Climatology Project (ISCCP) [*Schiffer and Rossow*, 1983; *Rossow and Schiffer*, 1999] typically includes 8 samples per day with geostationary coverage and 4 times per day from polar orbiters only. Optimally, we desire global coverage 6 times per day along with a plus or minus 6-min time simultaneity between cloud imager and radiation budget data. However, because of cost constraints, we will initially only be able to afford lidar and radar in single orbits.

In summary, practical limitations in the next several years will cause as many as three fundamental sampling limitations using current lidar and radar technologies and current science budget restrictions: (1) sampling nadir only, not full swath coverage as may be obtained with MODIS and CERES cloud and radiation data; this will greatly increase spatial sampling errors; fortunately, cloud layering is one of the most spatially contiguous of cloud properties; nevertheless, some sense of the added noise caused by nadir-only observations is required; (2) sampling on one satellite only; this problem will inevitably cause diurnal sampling errors because of the relatively large diurnal cycles present in both cloud properties and radiative fluxes; a good example is the tropical land and summer hemisphere land diurnal cycle of deep convection; another is the diurnal cycle of marine boundary layer clouds; (3) some lidar observations may be taken in orbits which cannot synchronize with the EOS Sun-synchronous orbits at 705 km orbital altitude. There are potentially two problems. First, orbit inclination determines the rate at which the satellite orbit precesses around the Earth's axis. For orbits inclined at 81° or 99° relative to the equatorial plane, the orbit precesses only once a year, and therefore remains synchronized to the local time of day at each equatorial crossing time. An orbit inclined at 57° (e.g., the ERBS spacecraft carrying the ERBE and SAGE II instruments) precesses almost exactly 5 times per year. As inclination angle decreases, the precession rate increases. The

Table 1. Orbital Characteristics of Proposed Satellite Missions Carrying Onboard Lidar or Radar Instruments

Satellite	Instrument	Launch Year	Inclination	Altitude
EOS-PM	CERES/MODIS	2000/2001	81°	705 km
ICESAT	lidar	2001	94°	600 km
PICASSO	lidar	none	80.5°	485 km
PICASSO/CLOUDSAT	lidar/radar	2003	80.5°	705 km

EOS PM is shown for reference.

TRMM spacecraft orbit inclined at 35° precesses 7.5 times per year. This means that the TRMM orbit changes the local time of day sampled by the ascending (south toward north) equator crossing of the orbit through a 24-hour period 7.5 times per year. A geostationary orbit has a 0° inclination and has a precession period that is defined by its orbital period. Since the orbital period increases with the altitude of the orbit, a geostationary orbit is simply the altitude at which the orbital period is equal to 1 day. The orbital period dependence on altitude, however, brings a second complication. Even if an orbit were matched in inclination to the EOS-PM orbit for example, if the orbital altitude is decreased to improve lidar and radar signal to noise ratio, then the orbital periods of the two spacecraft would no longer synchronize. In this case the two satellites will come into and out of phase with each other, with the phasing depending on the fractional difference in the orbital period. Note that the typical orbit period for an orbit altitude of 700 km is roughly 100 min. In summary, there are two orbital characteristics that will affect the ability to obtain "formation flying" with multiple spacecrafts: orbit inclination (i.e., local time of precession) and orbit altitude (i.e., orbital period).

There are three basic orbits that have been planned or proposed in the last several years to provide cloud lidar and or radar data to support studies of cloud layering in the radiative heating of the Earth and the atmosphere. The three satellites and their characteristics are given in Table 1. The EOS-PM orbit is also shown. Details of the orbital characteristics of the future satellite missions are provided in section 2. Given that there currently exists no global data set of multilayered cloud structures, how does one estimate the sampling errors caused by these different orbit possibilities for initial lidar/radar data sets? We propose in the current paper to utilize a state of the art global climate model containing prognostic cloud properties. Even this attempt is only a partial solution, but at this time is a reasonable way to start understanding the sampling error limitations of early cloud lidar and radar space-based systems. The goal of our experiment with the Colorado State University General Circulation Model (CSU GCM) is to quantify the impact of irregularly sampling in time and space radiation budgets and cloudiness, as is the case for measurements taken by onboard satellite instruments. Radiation- and cloudiness-related quantities simulated by the model will be later referred to as "true" diagnostics based on the fact that the CSU GCM provides uninterrupted regularly sampled diagnostics.

Section 2 provides technical information on the synchronization of the PICASSO and ICESAT satellites with EOS PM. Section 3 focuses on the design of the experiment with the CSU GCM. Because our results focus on longwave radiation budgets and cloudiness, we feel that it is important to provide a short description of the parameterizations of convective and large-scale condensation processes, cloudiness, and of the parameterization of radiative transfer at long and short wavelengths. This is done in section 4. Differences between monthly averaged satellite and true diagnostics of the TOA, ATM, and SFC longwave radiation budgets are discussed in section 5. The impact of the satellite sampling on cloudiness is described in section 6. Section 7 summarizes our findings and provides insights for the design of future satellite experiments.

2. Synchronization of Orbits

The present paper investigates the sampling errors for the three satellite orbits shown in Table 1. The three orbit scenarios can be summarized as follows: (1) PICASSO 705, synchronized 100% of the time with EOS PM; (2) PICASSO 485, synchronized 12% of the time with EOS PM; (3) ICESAT 600, synchronized 1.5% of the time with EOS PM.

The PICASSO 485 case is designed to show the loss in simultaneous data if the lidar or radar satellite altitude is reduced from the EOS 705 km altitude to a lower altitude of 485 km. While this lower altitude would be an advantage for lidar signal to noise ratios, it decreases by a factor of 8 the amount of data nearly simultaneous with EOS PM.

The ICESAT orbit is the least synergistic with EOS PM. This orbit is optimized for polar ice sheet sampling, and its precession period is almost exactly 2 years, so it matches the local ascending equator crossing times with EOS PM once every 2 years. Since the MODIS and CERES instruments on EOS PM are cross-track scanning, however, they see a range of local solar time east and west of the satellite that varies at the equator by the scanning width in degrees longitude divided by the 15° per hour the Earth rotates. For a 2000-km MODIS swath, this is roughly 20° longitude, or 1.3 hours of local solar time from the eastern to western edges of the scanning MODIS instrument. CERES scans a wider swath, but the majority of the CERES broadband flux data products are determined only when matched with MODIS data. In this case it turns out that the ICESAT satellite will orbit within the EOS-PM viewing swath for roughly 40 consecutive days, then return a year later (12 hours of precession in local time) to orbit within the EOS-PM swath for an additional 40 days. The satellite only requires precession through 12 hours of local time because the satellite orbits view both day and night sides of the planet with each orbit. Because the ICESAT lidar orbit is at a different orbit altitude, however, only about 12% of the 40 days will contain data which are simultaneous within plus or minus 6 min of the EOS-PM orbit. For the 705-km EOS-PM orbit altitude the orbital period is roughly 100 min. The ICESAT 600-km orbit period is 96.8 min. In this case, the ICESAT and EOS-PM orbits will remain synchronized with plus or minus 6 min for ~9 hours and will resynchronize every 3.2 days. In summary, the ICESAT and EOS-PM orbital data are

synchronized to plus or minus 6 min ~12% of 40 days, or roughly 5 days worth of orbits every year. Because the precession period of the ICESAT orbit is 2 years, these 5 days of simultaneity will occur in essentially the same month of the year each year. Because EOS AM is a 1030 LT Sun-synchronous orbit, the ICESAT orbit will also synchronize with this orbit for 5 days each year. The 5 days with EOS-AM will be shifted by 3 months from the 5 days with EOS PM. This is the time it will take ICESAT to precess through 3 hours of local time at 1 hour per month.

The three satellite orbits have been simulated, along with the EOS-PM orbit, for a nominal 5-year period. For simplicity we assume that the ICESAT orbit synchronizes in local time with EOS PM in July, one of the most interesting periods for multilayered clouds in the Northern Hemisphere summer. The EOS-PM MODIS scanner swath is used to determine the region of the Earth viewed by EOS PM. For each of the three test cloud lidar and radar orbits, we keep track of all GCM grid boxes for which the nadir lidar or radar beam would have viewed a portion of the EOS-PM MODIS swath within plus or minus 6 min of the EOS-PM time. This GCM grid box is considered to have been perfectly measured by the combination of the EOS-PM and lidar or radar observations. All other GCM grid boxes are considered to be "unsampled" by the satellite orbit. The time discretization of the GCM grid data is hourly. The GCM spatial grid is 4° latitude by 5° longitude. Since orbital periods are roughly 100 min, there is no possibility of viewing the same hourly grid box more than one time. The orbit simulations then provide a simple on/off designation for each hourly GCM grid box: sampled or not sampled by the synchronized EOS PM and lidar and radar observations. Sampling errors are determined by comparing the true GCM fields for any cloud or radiation parameters (all 24 hours for each grid box) with the subsampled GCM fields which include only the time of near-simultaneous observation by the combined EOS PM and cloud lidar or radar mission. Note that in principle a "perfect" satellite system in this simulation would require 12 satellite orbits (24 samples per day) with each orbit synchronized between the passive and the active cloud remote sensing data across the full swath of MODIS. Even the PICASSO 705 km orbit cannot meet this test.

Previous studies using ISCCP cloud layering data [*Charlock et al.*, 1994] have tried varying assumptions about cloud layer overlap, including maximum, random, and minimum overlap in order to do sensitivity studies of the effect of cloud overlap on radiative heating. These studies have shown that the largest effects of cloud overlap are found for downward surface longwave fluxes and on vertical profiles of longwave heating rates within the atmosphere. The present study will focus on the sampling of these fields for future measurements of cloud layer overlap in conjunction with cloud optical properties and radiative fluxes at the top of the atmosphere. This combination should lead to a great improvement in the rigor in estimating longwave fluxes at the surface and within the atmosphere.

While the ICESAT sampling clearly allows only a very limited amount of time that is simultaneous with EOS AM and EOS PM (e.g., 1.5% of the time for each satellite), it nevertheless will still be extremely useful for initial global studies of multilayered clouds. It will also allow collection of some cloud-layering data at varying times of the day. Unfortunately, because of the slow precession period (24 hours in 2 years), it will not be possible to unscramble the seasonal cycle from the diurnal cycle using the ICESAT data. For example, if ICESAT is launched in June at a local time of 1330 equator crossing, each successive June with ICESAT data set will sample at 1330. July will sample at 1430, August at 1530. The strong convective diurnal cycle of cloud layering in the Northern Hemisphere summer will not be seen by this data set. Nevertheless, ICESAT will provide critical cloud-layering data, especially over the polar regions where imager-derived cloud properties are extremely uncertain. In this case, the diurnal cycles are small, the ICESAT will thoroughly sample the polar regions.

The orbits for the PICASSO and CloudSAT missions recently selected as part of the NASA Earth System Science Pathfinder (ESSP) Program were not restricted to the ICESAT orbit and chose instead to nearly match the EOS-PM orbit inclination. In particular, an inclination angle just slightly different than EOS-PM was chosen in order to slowly precess from the eastern side of the EOS-PM orbit swath at 1410 local solar time at the beginning of the mission to the western side of the EOS-PM orbit swath at 1250 local solar time by the end of the mission. This slow precession keeps synergism of the two spacecraft orbit planes, while allowing the lidar or radar to validate the complete range of MODIS cloud property retrievals as a function of the viewing zenith angle and solar azimuth angle. It also allows matching of the EOS-PM and ESSP platform local time of day sampling for all 12 months of the year, for each year of the mission. The final step in orbital matching by CloudSat and PICASSO is to fly at an orbit altitude of 705 km, thereby achieving 100% of the lidar data synchronized with plus or minus 6 min of the EOS-PM MODIS and CERES data for optical cloud properties and radiative fluxes. Even the PICASSO and CloudSat missions, however, still view only at nadir, so spatial sampling errors will still be much larger than encountered using EOS AM and/or EOS PM.

3. Design of Experiment

The objective of this study is not to compare the top-of-the-atmosphere (TOA), atmospheric (ATM), and surface (SFC) longwave radiative budgets, and the cloudiness and its optical properties simulated by the CSU GCM against satellite-derived observations. The goal of this experiment is in using the CSU GCM to quantify the impact of irregularly sampled in time and space radiation budget and cloud characteristics, as is the case for measurements taken by onboard satellite instruments. Radiation- and cloudiness-related quantities simulated by the model will be later referred to as "true" diagnostics based on the fact that the CSU GCM provides an uninterrupted hourly sampling, and simulated monthly averages are computed from exactly 720 samples at each model grid box for a 30-day month. "Satellite" diagnostics will refer to diagnostics obtained by the model when a mask that tracks the location of coincident grid points between the ICE SAT and the PICASSO satellites and the EOS-PM platform is applied at a specific GMT time. Unlike with the CSU GCM, the number of satellite samplings accumulated over a month varies between neighboring model grid points and is, of course, less than the total number of hours per month. Monthly averaged satellite diagnostics are obtained by dividing their accumulated sum by the number of samplings per month and not by the total number of hours per month as is done for true diagnostics.

Time series of the latitudinal and longitudinal coordinates of coincident locations between the EOS-PM platform and ICESAT flying at the altitude of 600 km, and between the

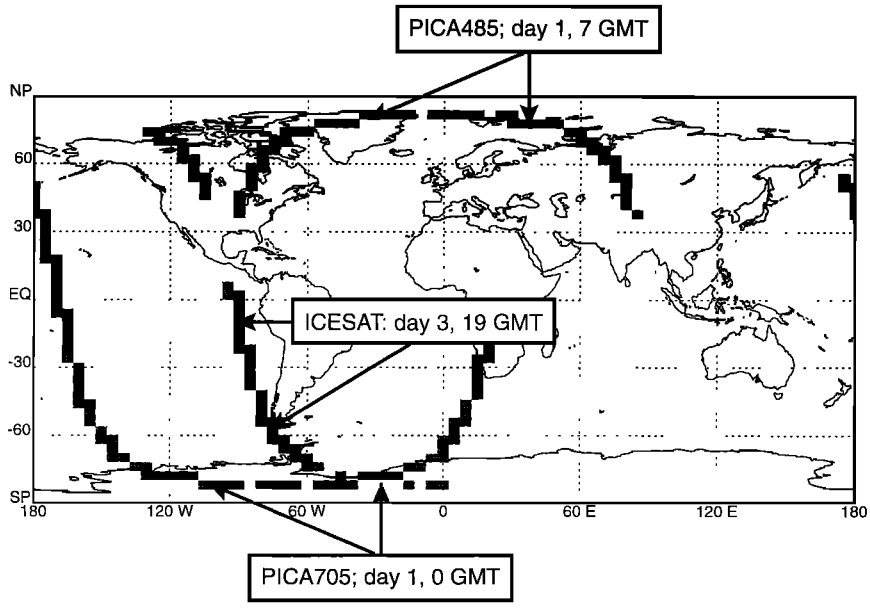

Figure 1. ICESAT, PICA485, and PICA705 orbit tracks simulated for the first day and first hour that coincident grid points exist for July 2001.

EOS-PM platform and PICASSO flying at the altitudes of 485 km (later referred to as PICA485) and 705 km (later referred to as PICA705), were created for the time period between July 1, 2001 and June 31, 2006. Each time series was later spatially gridded onto the 4° in latitude by 5° in longitude horizontal resolution of the CSU GCM and temporarily gridded onto the hourly time step used for the parameterizations of shortwave and longwave radiation, cloud fraction, and cloud optical properties. In doing so, we produced three 5-year time series of hourly global maps of a flag that marked the presence or absence of coincident grid points among ICESAT, PICA485, and PICA705 carrying a lidar or a radar, and the EOS-PM platform carrying conventional passive instruments. For simplicity, we will later refer to these time series of coincident grid points as "orbits." These three orbits were simulated in the CSU GCM independently. Figure 1 illustrates the instantaneous orbit track simulated by ICESAT, PICA485, and PICA705 within the first hour the ICESAT orbit and the PICASSO 485 km and PICASSO 705 km orbits cross the EOS-PM orbit for July 2001 at the spatial resolution of the CSU GCM. As already discussed in section 2, there is an obvious increase in the number of coincident grid points in PICA705 relative to ICESAT and PICA485, due to the same altitude and similar inclination between the PICASSO 705 km and the EOS-PM orbits.

Plate 1 shows latitude versus time cross sections of the number of accumulated coincident grid points for ICESAT, PICA485, and PICA705 over the entire simulation. Plate 2 shows the number of coincident grid points accumulated during the month of July 2001 for ICESAT (top), PICA485 (middle), and PICA705 (bottom).

As already discussed in section 2, the ICESAT and EOS-PM orbits are synchronized for roughly 40 consecutive days per year. When a July 1, 2001, launch date is assumed, ICESAT yields an approximate global coverage of coincident grid points between the months of July and September each year. In addition, the month during which the best synchronization between the two satellites occurs drifts from July 2001, to August 2003, to September 2005, in conjunction with the every 2-year precession period of the ICESAT satellite. Synchronization between PICA485 and EOS PM is very similar to that between ICESAT and EOS PM, but in contrast to ICESAT, synchronization is maintained through a major part of the 60-month simulation, due to the increased inclination of the orbit relative to that of EOS PM. As seen in Plate 2, the number of satellite overpasses decreases rapidly past July 2004 for PICA485, as the orbit precesses out of the MODIS-scanning swath. This affects equatorial latitudes first before affecting all latitudes between 60°N and 60°S by the end of the simulation. Nominal lifetime of the PICASSO and CloudSat missions is between 2 and 3 years. Planned launch of PICASSO and CloudSat are in March 2003. The launch of July 2001 shown in the GCM simulation study is used to simplify direct comparison of all the sampling errors for the different orbit scenarios.

Plate 2 shows that the ICESAT and PICA485 orbits yield similar geographical distributions of the number of accumulated coincident grid points during July 2001. That number of coincident grid points is less than 4 over a major part of the globe except at high latitudes.

The impact of the change in the satellite altitude from 485 to 705 km between PICA485 and PICA705 is well seen in Plates 1 and 2. By increasing its altitude from 485 to 705 km the PICASSO satellite maintains a synchronization 100% of the time with EOS PM during the entire simulation. As a result, the number of satellite overpasses accumulated per month remains relatively constant from one month to the next at least until July 2004, as seen in Plate 1. In addition, Plate 1 reveals that the number of accumulated coincident grid points shows little variation between model grid boxes, at least between 60°N and 60°S. Over a major portion of the globe, this number is greater than 12, which is over a factor of 4 greater than that obtained with either PICA485 and ICESAT. Out of the three orbits, PICA705 provides the best spatial and temporal samplings over the July 2001 to June 2006 time period, from which

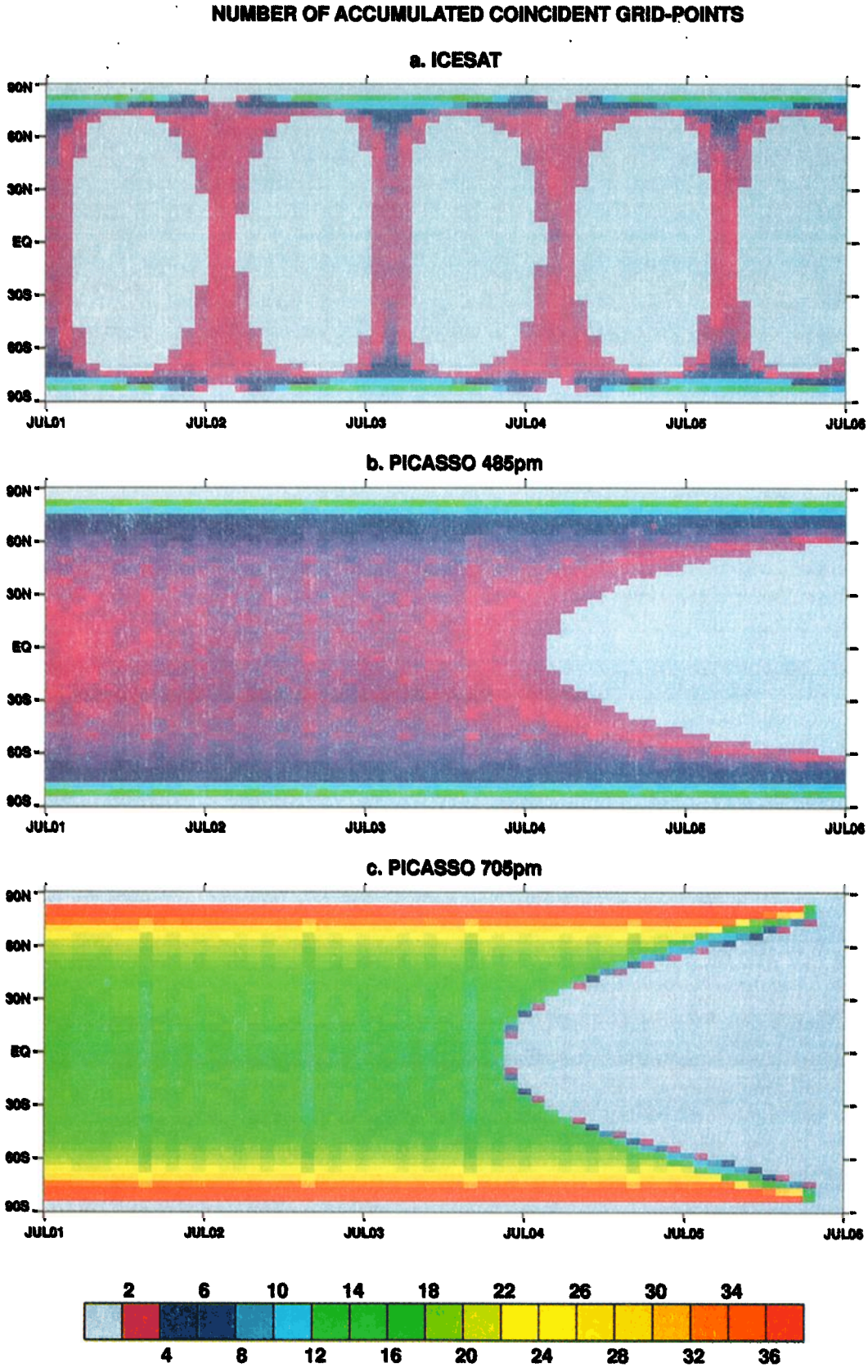

Plate 1. Latitude versus time cross sections of the zonally averaged number of accumulated coincident grid points for (a) ICESAT, (b) PICA485, and (c) PICA705. The bottom axis marks the beginning of each simulated year, JUL01 corresponding to July 1, 2001.

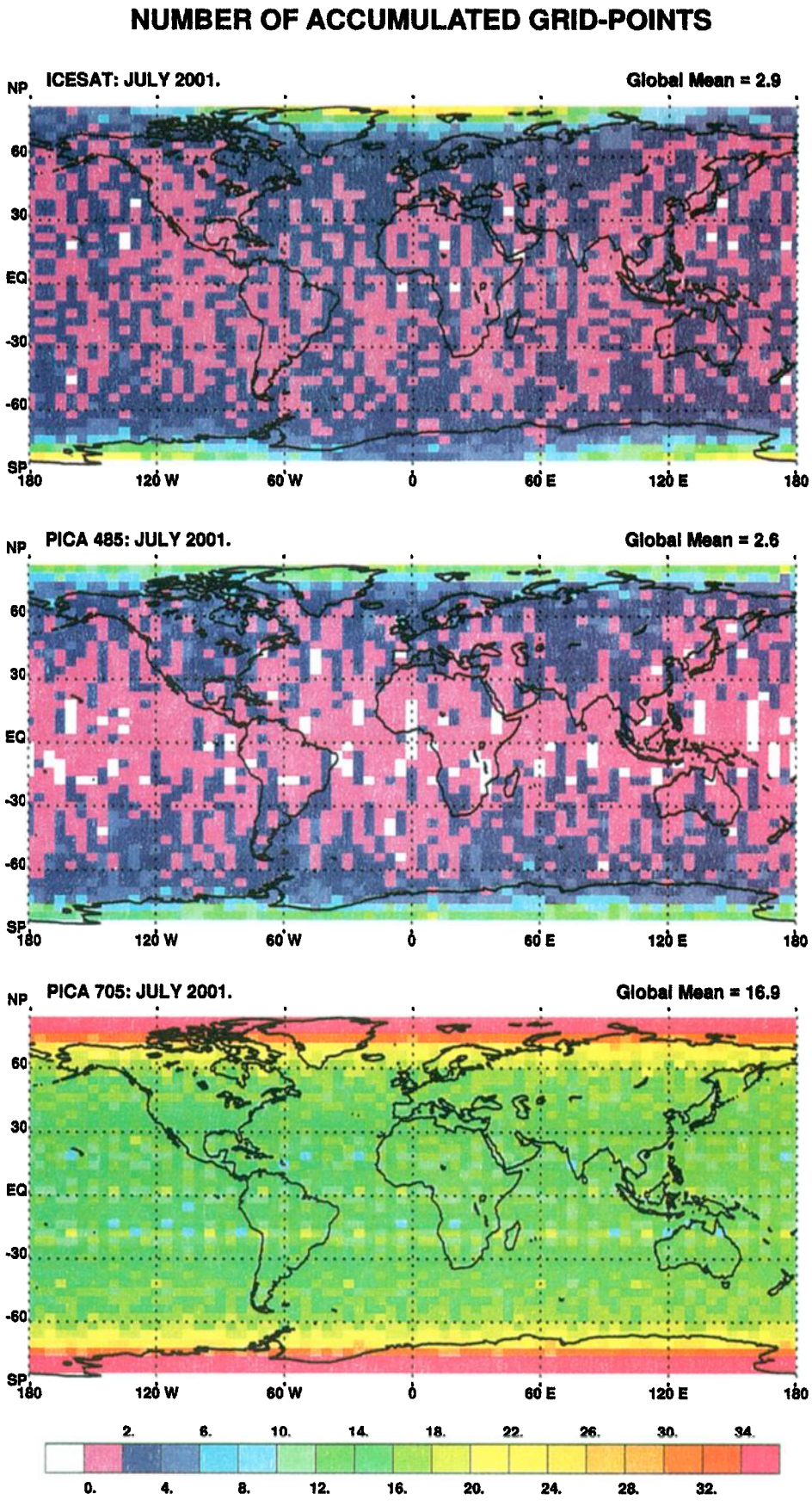

Plate 2. Geographic distributions of the number of accumulated coincident grid points for ICESAT, PICA485, and PICA705 for July 2001.

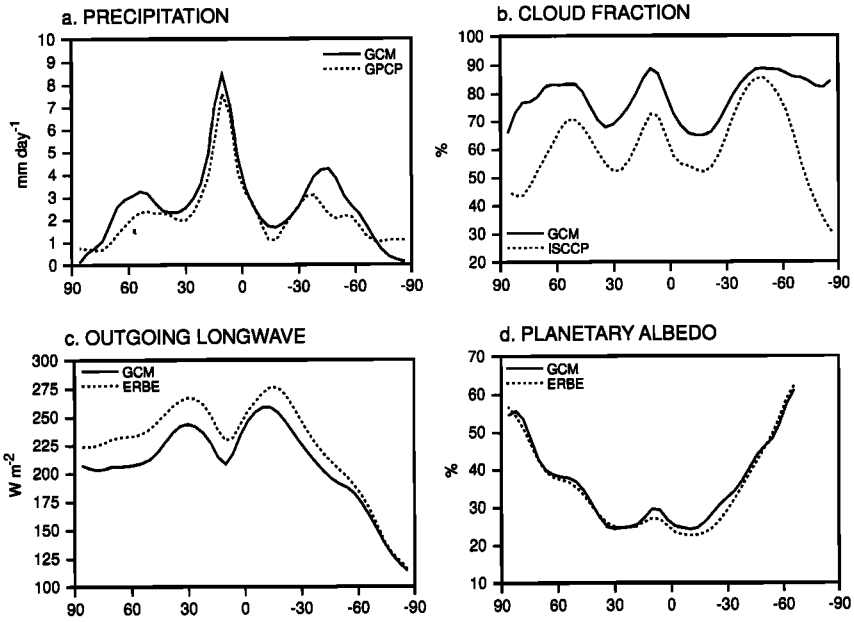

Figure 2. Zonally averaged profiles of (a) precipitation, (b) cloud fraction, (c) outgoing longwave radiation, and (d) planetary albedo simulated with the CSU GCM against data in July.

we expect the smallest differences between satellite and true diagnostics.

4. CSU GCM

The CSU GCM is a 17-level grid point model with a horizontal resolution of 4° in latitude and 5° in longitude. The vertical discretization is based on a modified σ coordinate in which the planetary boundary layer (PBL) is the bottom layer of the model [*Suarez et al.*, 1983].

The parameterization of convection is a revised version of the Arakawa-Schubert scheme [*Arakawa and Schubert*, 1974] and includes an ice phase [*Lord*, 1978]. A prognostic closure through the introduction of a prognostic equation of the vertically integrated cumulus kinetic equation [*Pan and Randall*, 1998] replaces the quasi-equilibrium assumption of the cloud work function. Convection is not restricted to start at the top of the PBL but may also start at any level in the free troposphere through the inclusion of a linear profile of the normalized mass flux [*Ding and Randall*, 1998]. The parameterization of large-scale cloud microphysical processes follows *Fowler et al.* [1996] and includes five prognostic equations for the mass of water vapor, cloud water, cloud ice, rain, and snow. Parameterized cloud microphysical processes follow *Rutledge and Hobbs* [1983] and *Lin et al.* [1983] for the warm and cold phases, respectively.

The parameterization of longwave and shortwave radiative transfer processes is described by *Harshvardhan et al.* [1987]. At long wavelengths the upward and downward clear-sky longwave fluxes are computed using the broadband absorptivity concept. Broadband absorption and emission by H_2O [*Chou*, 1984], CO_2 [*Chou and Peng*, 1984], O_3 [*Rodgers*, 1968], and the water vapor continuum [*Roberts et al.*, 1976] are included. Cloudy fluxes are obtained by computing the probability of a clear line of sight between each model layer and all other layers, the ground, and the top of the atmosphere. At short wavelengths the computation of clear-sky fluxes follows *Lacis and Hansen* [1974] for the molecular absorption by H_2O, CO_2, and O_3. Assuming that the optical properties of a cloudy layer are known, cloudy fluxes are computed using the delta-Eddington approximation [*Joseph et al.*, 1976].

The CSU GCM does not include a parameterization of fractional cloudiness at this time. For PBL clouds, the cloud fraction follows the formulation of *Harshvardhan et al.* [1989]; it is assumed to be 1 when PBL clouds are more than 12.5 hPa deep and decreases linearly to zero as their pressure thickness decreases from 12.5 hPa to zero. Above the PBL, clouds are assumed to form when and where the total amount of condensate exceeds 10^{-5} kg kg^{-1}. Their cloud fraction is set equal to 1. This finite threshold is necessary to hinder the formation of optically very thin upper tropospheric clouds. The optical properties of clouds are interactive and depend upon the cloud water, cloud ice, and snow paths [*Fowler and Randall*, 1996]. The optical depth and infrared emissivity of clouds follow the formulations of *Stephens* [1978] and *Harshvardhan* [1989], respectively.

ICESAT, PICA485, and PICA705 produce realistic simulations of sampling biases to the extent that the CSU GCM produces realistic simulations of, in particular, precipitation, cloudiness, and the TOA radiative budget. Because we focus our discussion on differences between satellite and true diagnostics, deficiencies in the simulated climate should not affect the magnitude of the simulated sampling bias. Instead, deficiencies in the geographical distribution of the true diagnostics will affect the geographical distribution of the sampling bias, relative to the one that would actually be obtained with the satellites. Anyhow, it is important to summarize the performance of the CSU GCM to simulate climate. Figure 2 summarizes a few characteristics of the simulated climate. Weaknesses in the simulated climate are similar to the ones discussed by *Fowler et al.* [1996] and *Fowler and Randall* [1996]. The CSU GCM overestimates precipitation at tropical and extratropical latitudes when compared against the Global Pre-

Table 2. List of Longwave Radiation and Cloudiness Diagnostics Saved for Each Satellite Orbit and the True Orbit

Diagnostics	Acronym	Units
TOA all-sky outgoing longwave radiation	TOAlw	W m^{-2}
TOA clear-sky outgoing longwave radiation	$TOAlw_{cl}$	W m^{-2}
TOA cloud longwave radiative forcing	TOAlwcrf	W m^{-2}
SFC all-sky net longwave radiation	SFClw	W m^{-2}
SFC clear-sky net longwave radiation	$SFClw_{cl}$	W m^{-2}
SFC cloud longwave radiative forcing	SFClwcrf	W m^{-2}
ATM all-sky net longwave radiative heating	ATMlw	W m^{-2}
ATM clear-sky net longwave radiative heating	$ATMlw_{cl}$	W m^{-2}
ATM cloud longwave radiative heating	ATMlwcrf	W m^{-2}
Frequency of occurrence of clear sky	Fclr	%
Frequency of occurrence of clouds	Fcld	%
Frequency of occurrence of water clouds	Fwcld	%
Frequency of occurrence of ice clouds	Ficld	%
Frequency of occurrence of mixed-phase clouds	Fmcld	%
Frequency of occurrence of cloud overlap	Fovlp	%
Accumulated cloud optical depth	Foptd	(per hPa)

TOA, SFC, and ATM refer to top-of-the-atmosphere, surface, and atmospheric variables.

cipitation Climatology Project [*Huffman et al.*, 1997] (GPCP) data in July. The increased simulated cloud fraction relative to that observed by ISCCP [*Schiffer and Rossow*, 1983; *Rossow and Schiffer*, 1999] yields a decreased TOA outgoing longwave radiation and an increased planetary albedo when compared against the Earth Radiation Budget Experiment [*Barkstrom and Smith*, 1986] (ERBE) data, as seen in Figure 2. Maps of the TOA outgoing longwave radiation would show that in the tropics the CSU GCM overestimates the intensity of convection along the Intertropical Convergence Zone (ITCZ) over the oceans, in particular, over the western Pacific and Indian Oceans. In the middle latitudes the model underestimates the TOA outgoing longwave radiation in the summer hemisphere, in particular, over the continents. Geographical distributions of the planetary albedo would show that the CSU GCM overestimates the planetary albedo over the continents in both hemispheres. Maps of the TOA outgoing longwave radiation and planetary albedo are omitted here for brevity.

One goal of flying the PICASSO and ICESAT satellites in formation with EOS PM is to obtain simultaneous information of the radiative properties and layering of clouds. This kind of simultaneous data is sorely needed and would greatly help the modeling community improve parameterizations of tropical and extratropical cloud systems in GCMs. To date, very few studies have been published on the vertical structure of clouds due to, in part, the lack of observations against which simulations can be compared. However, the treatment of vertically varying cloud fraction in GCMs is important because it influences not only the distribution of longwave and shortwave radiative heating rates [*Geleyn and Hollingsworth*, 1979; *Morcrette and Fouquart*, 1986] but also evaporation of precipitation [*Jakob and Klein*, 1999]. *Fowler and Randall* [1999] compare the climatology of upper tropospheric clouds simulated with the CSU GCM against ISCCP-D1 cloud products [*Rossow and Schiffer*, 1999]. Using the Lidar in-Space Technology Experiment (LITE) [*McCormick et al.*, 1993] data, *Fowler and Randall* [1999] demonstrate that the difficulty in simulating optically thin upper tropospheric clouds results because the simulated geometrical thickness of cloudy layers is too coarse relative to observations. Global observations of multilayered cloud systems, as planned by the PICASSO-CENA and CloudSat missions, will help the modeling community identify deficiencies in current parameterizations of microphysical and radiative properties of clouds.

5. Impact of Sampling on Radiative Budgets

A large number of monthly averaged diagnostics related to cloud properties, all-sky and clear-sky net longwave radiation, and cloud longwave radiative forcings simulated at the top of the atmosphere, in the atmosphere, and at the surface were saved for each orbit simulation and compared against the true simulation. Table 2 provides a list of those diagnostics and their acronyms.

5.1. Regional Sampling

Table 3 provides a summary of the sampling bias attached to each monthly averaged longwave radiation diagnostic obtained with PICA705, PICA485, and ICESAT for July 2001. In Table 3 the bias is defined as the globally averaged difference between monthly mean diagnostics obtained with either satellite orbit and the true diagnostics. It is a measure of the impact of poorer diurnal sampling in the PICA705, PICA485, and ICESAT simulations relative to the hourly sampling in the true simulation with the CSU GCM, at individual model grid points. We define σ to be the standard deviation of the sampling bias at individual grid points, computed from the global mean bias. It is a measure of the spatial variability of the bias due to the irregular geographical distribution of coincident satellite overpasses between model grid points.

Looking at Table 3 reveals that for the three satellite orbits, diagnostics of the net longwave radiation at the surface display the largest biases, whereas diagnostics in the atmosphere and at the top of the atmosphere display smaller biases. The decreased bias between diagnostics of the net longwave radiation at the surface and the top of the atmosphere is true under both all-sky and clear-sky conditions, indicating that the magnitude of the bias is more strongly influenced by the diurnal cycle of the surface temperature than that of the atmospheric temperature, water vapor, and cloudiness, even at the top of the atmosphere. It is interesting to note that in the three simulations the biases in SFClw and $SFClw_{cl}$ have about the same magnitude, while the biases in $TOAlw_{cl}$ are systematically less than those calculated for TOAlw, and the biases in $ATMlw_{cl}$

Table 3. Regional Sampling Errors of Longwave Radiation Diagnostics for July 2001

GCM Diagnostics	Units	PICA705		PICA485		ICESAT	
		Bias	σ	Bias	σ	Bias	σ
TOAlw	W m^{-2}	1.05	7.11	1.55	21.83	1.06	19.06
TOAlw$_{cl}$	W m^{-2}	0.75	2.02	0.91	5.57	0.88	5.70
TOAlwcrf	W m^{-2}	−0.30	6.53	−0.64	19.77	−0.19	17.26
SFClw	W m^{-2}	1.99	8.57	2.42	24.57	2.67	23.67
SFClw$_{cl}$	W m^{-2}	1.97	6.36	2.36	16.64	2.62	17.21
SFClwcrf	W m^{-2}	−0.02	4.95	−0.06	14.73	−0.05	13.64
ATMlw	W m^{-2}	0.94	7.92	0.87	22.30	1.61	21.12
ATMlw$_{cl}$	W m^{-2}	1.22	4.83	1.45	13.00	1.74	13.04
ATMlwcrf	W m^{-2}	−0.28	6.21	−0.58	18.25	−0.13	16.80

The description of each GCM diagnostic is given in Table 2.

are systematically greater than those calculated for ATMlw for the three orbits. For instance, PICA705 gives a global bias error equal to 0.75 W m^{-2} for TOAlw$_{cl}$ compared to 1.05 W m^{-2} for TOAlw (and a global bias error equal to 0.94 W m^{-2} for ATMlw$_{cl}$ compared to 1.22 W m^{-2} for ATM), while at the surface, the biases in SFClw and SFClw$_{cl}$ are equal to 1.99 W m^{-2} and 1.97 W m^{-2}, respectively. At the surface the diurnal cycle of the surface temperature contributes a major part to the magnitude of the global mean bias in the net longwave radiation, under both clear-sky and cloudy conditions. At the top of the atmosphere and at the surface, clouds are primarily responsible for the decreased bias between all-sky and clear-sky fluxes. Note that the bias in ATMlw is less than that in ATMlw$_{cl}$, while it is larger in SFClw and TOAlw than in SFClw$_{cl}$ and TOAlw$_{cl}$, respectively.

Although of different magnitude, the three orbit simulations yield an overestimation of the monthly averaged all-sky and clear-sky longwave radiation diagnostics when compared against monthly averaged diagnostics obtained with the model. A decreased value of the bias between the surface and the top-of-the-atmosphere results because the diurnal cycle of longwave radiation is greater at the surface than at the top of the atmosphere, in conjunction with the diurnal cycle of the surface temperature. Over land and desert regions the diurnal variation of TOAlw$_{cl}$ and SFClw$_{cl}$ can be modeled as half-sine curves, nearly constant at night, then increasing sharply after dawn to peaking near noon, then decreasing rapidly to shortly after dusk [*Young et al.*, 1998]. This correction is not included in the current sampling analysis, and therefore the near-noon EOS-PM orbit causes a positive bias in global mean flux.

To illustrate our results, Figure 3 shows the geographical distribution of the bias in SFClw$_{cl}$ obtained with ICESAT, PICA485, and PICA705 for July 2001. We choose SFClw$_{cl}$ to highlight the impact of the diurnal cycle of the surface temperature on the geographical distribution of the sampling bias. The monthly averaged distribution of SFClw$_{cl}$ simulated with the CSU GCM is also shown for reference (top left).

In the summer hemisphere, there exists a sharp contrast in the magnitude of SFClw$_{cl}$ between land and oceans in the middle latitudes due to the decreased diurnal cycle of the sea versus land surface temperatures, the largest SFClw$_{cl}$ being observed, of course, over desert regions. In the tropics, increased downward longwave emission by water vapor, also known as the water vapor greenhouse effect, contributes a major part to the decrease in SFClw$_{cl}$ over both land and oceans. In the winter hemisphere the downward longwave emission of the dry and cold troposphere is too small to counteract the surface longwave emission. As a result, SFClw$_{cl}$ simulated over the Southern Oceans is as large as over some regions of the summer hemisphere, despite colder surface temperatures.

In contrast to that obtained with ICESAT and PICA485 the sampling bias in SFClw$_{cl}$ obtained with PICA705 is less noisy and displays smaller differences between land and oceans. Over the oceans the difference in SFClw$_{cl}$ between the PICA705 and the CSU GCM is mostly negative and in the order of −4.2 to +4.2 W m^{-2}. Over land, SFClw$_{cl}$ simulated with PICA705 is overestimated relative to the true diagnostic simulated with the CSU GCM. The magnitude of the sampling bias is in the order of 4.2 to 12.6 W m^{-2} over most of the continents, with values in excess of 12.6 to 20.9 W m^{-2} over the major desert regions, as seen over the Tibetan Plateau, and the Saharan and Australian deserts. Comparing the geographical distribution of SFClw$_{cl}$ simulated with the CSU GCM against that of the bias in SFClw$_{cl}$ obtained with PICA705 shows that the sampling bias is the greatest over areas of high clear-sky net longwave radiation. This effect results, of course, because of the poorer sampling of the diurnal cycle of net longwave radiation in PICA705 than in the true simulation. As seen in Plate 2, the number of coincident grid points accumulated for the month of July 2001 is about constant between 60°N and 60°S. It is, in particular, because that number remains constant that the difference in the magnitude of the bias in SFClw$_{cl}$ between land and oceans can be so clearly captured and attributed, for a major part, to the decreased diurnal cycle sampling between the PICA705 and the true model simulation. In contrast to PICA705, Plate 2 reveals that in ICESAT and PICA485, not only is the number of satellite overpasses decreased relative to PICA705 but also the number of overpasses is significantly different between neighboring grid points. As a result, the land-oceans contrast in the magnitude of the bias in SFClw$_{cl}$ simulated in ICESAT and PICA485 is not so well seen as in PICA705. For instance, the bias in SFClw$_{cl}$ simulated in ICESAT over North and South America is negative, and its absolute magnitude is much larger and of the opposite sign than that simulated in PICA705. Although the globally averaged biases do not strongly vary between PICA705 (2.0 W m^{-2}), ICESAT (2.6 W m^{-2}), and PICA485 (2.3 W m^{-2}), there exist significant regional differences between the three orbit simulations. In general, the geographical distribution of the bias simulated in ICESAT and PICA485 is noisier than that simulated in PICA705, the land versus oceans contrast is not clearly depicted, and regional maxima in the bias are strongly enhanced in ICESAT and PICA485 relative to PICA705, as

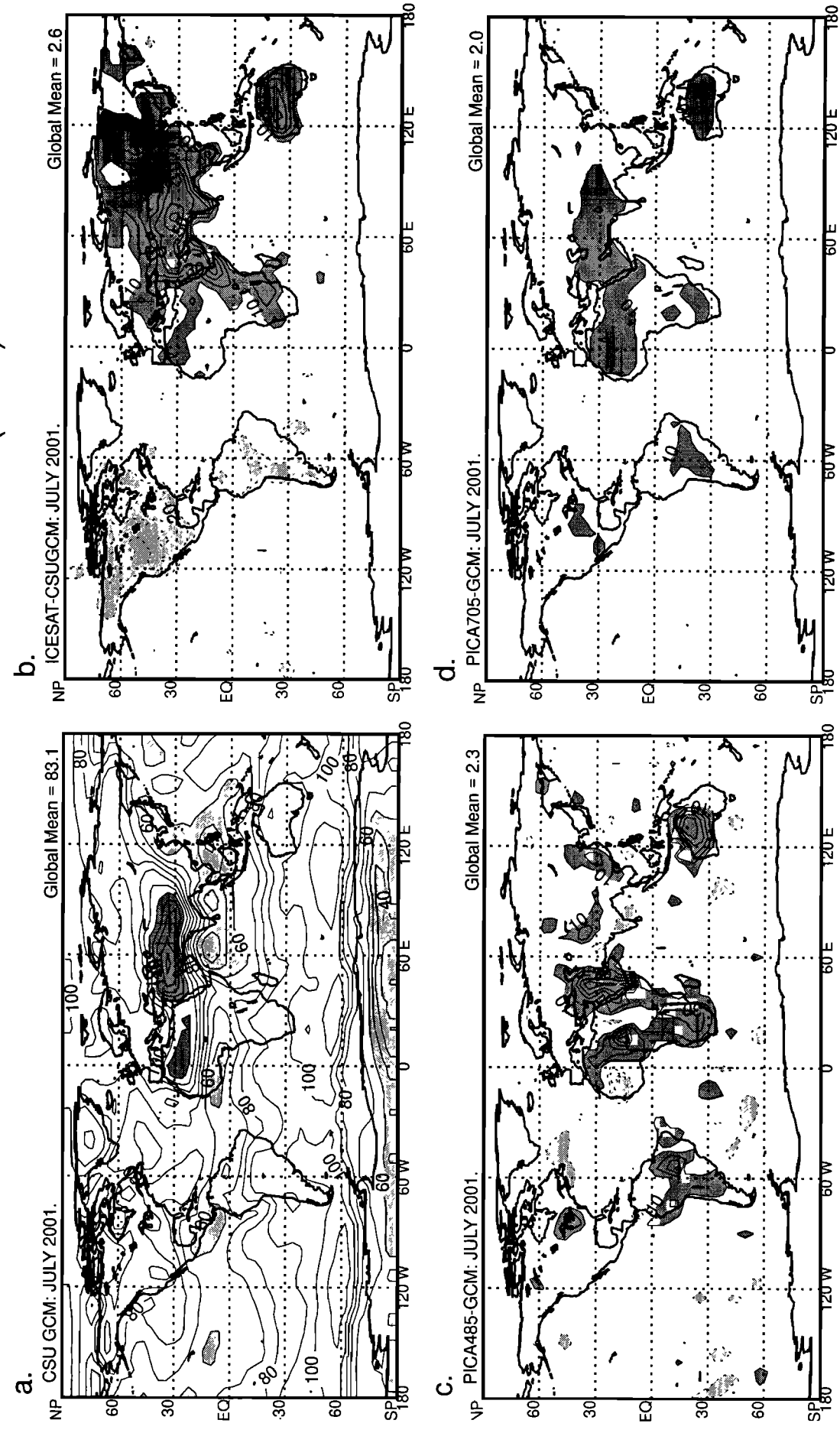

Figure 3. Monthly averaged geographical distributions of (a) the SFC clear-sky net longwave radiation ($SFClw_{cl}$) simulated with the CSU GCM, (b) the difference in $SFClw_{cl}$ between the ICESAT and the GCM, (c) the difference in $SFClw_{cl}$ between the PICA485 and the CSU GCM, and (d) the difference in $SFClw_{cl}$ between the PICA705 and the CSU GCM. In Figure 3a, contour intervals are every 10 W m^{-2}. Areas below 60 W m^{-2} are shaded in light gray, and areas above 120 W m^{-2} are shaded in dark gray. In Figures 3b, 3c, and 3d, contour intervals are every 10 W m^{-2}. Areas below 10 W m^{-2} are shaded in light gray, and areas above 10 W m^{-2} are shaded in dark gray.

Table 4. Zonal Mean Sampling Errors of Longwave Radiation Diagnostics Between July 2001 and June 2006

GCM Diagnostics	Units	PICA705		PICA485		ICESAT	
		Bias	σ	Bias	σ	Bias	σ
TOAlw	W m^{-2}	0.93	1.45	0.97	3.77	0.32	5.30
TOAlw$_{cl}$	W m^{-2}	0.69	1.26	0.74	1.36	0.19	3.52
TOAlwcrf	W m^{-2}	−0.24	1.02	−0.22	3.26	−0.13	4.35
SFClw	W m^{-2}	1.75	2.65	1.89	4.81	0.004	10.29
SFClw$_{cl}$	W m^{-2}	1.54	2.55	1.73	3.50	0.03	8.81
SFClwcrf	W m^{-2}	−0.22	0.82	−0.16	2.64	0.02	4.23
ATMlw	W m^{-2}	0.83	1.99	0.93	4.41	−0.32	8.12
ATMlw$_{cl}$	W m^{-2}	0.85	1.54	0.98	2.57	−0.16	6.21
ATMlwcrf	W m^{-2}	−0.021	0.95	−0.06	3.15	−0.16	4.44

observed over the Himalayan Plateau. In addition to the small number of satellite overpasses which affects a proper sampling of the diurnal cycle at individual grid points, the uneven number of overpasses between adjacent grid points contributes a major part to the increased noisiness of the sampling bias. One interesting feature to note is the sign change between the bias observed over the Himalayan and Tibetan Plateaus and observed over North and South America in ICESAT and, to a lesser extent, in PICA485. This sign change can be attributed to the difference in the surface temperature, and the atmospheric profiles of temperature and water vapor, as well as in the number of accumulated coincident grid points between the two areas. The difference in surface and atmospheric conditions yields a decrease in SFClw$_{cl}$ over the American continents, as seen in the CSU GCM map in Figure 3. At least over the western part of the United States, the number of accumulated coincident grid points is 2 times less than that observed over a major part of the Himalayan Plateau, as seen in Plate 2. Comparing maps of the sampling bias in SFClw$_{cl}$ and TOAlw$_{cl}$ would illustrate the reduced effect of the diurnal cycle of the surface temperature on the magnitude of the sampling bias between the surface and the top-of-the-atmosphere. In PICA705, PICA485, and ICESAT, geographical patterns of the sampling bias in TOAlw$_{cl}$ are the same as in SFClw$_{cl}$, but the magnitude of the sampling bias is strongly reduced.

Let us now focus on the difference in σ among the three orbit simulations. As for biases, the σ values of net longwave radiation fluxes are greater at the surface than in the atmosphere and at the top of the atmosphere, for both clear-sky and all-sky conditions. This finding makes sense because the greater the sampling biases, the greater the σ values should be expected. In PICA705 the decrease in the bias of clear-sky net longwave radiation from 1.97 W m^{-2} at the surface to 1.05 W m^{-2} at the top of the atmosphere is observed in conjunction with a decrease in σ from 6.36 to 2.02 W m^{-2}. As already noted with sampling biases, σ values of clear-sky net longwave radiation diagnostics are less than that of all-sky diagnostics.

While sampling biases provide quantitative estimates of the impact of the decreased diurnal sampling in the satellite orbit simulations when compared against the true model simulation, σ values provide estimates of the spread in the magnitude of the bias between individual grid points. In PICA705, results suggest that σ values can be explained in terms of the difference in the bias between land and oceans which results because of the impact of diurnally varying land surface temperature relative to climatologically fixed sea surface temperatures. In ICESAT and PICA485 the irregular distribution in the number of satellite overpasses between grid points contributes a major part to an enhanced σ among PICA705 and ICESAT and PICA485. The magnitude of σ of all longwave radiation diagnostics increases significantly as the number of accumulated coincident grid points decreases, as shown in Table 3. The σ in TOAlw (TOAlw$_{cl}$) increases from 7.11 W m^{-2} (2.02 W m^{-2}) in PICA705 to 21.83 W m^{-2} (5.57 W m^{-2}) in PICA485 and 19.06 W m^{-2} (5.70 W m^{-2}) in ICESAT, in response to a factor of 8 decrease in the number of coincident grid points between PICA705 and either PICA485 or ICESAT.

Finally, Table 3 reveals a large decrease in the magnitude of σ between all-sky and clear-sky diagnostics at the surface, in the atmosphere, and at the top of the atmosphere. For instance, σ decreases from 7.11 W m^{-2} to 2.02 W m^{-2} between TOAlw and TOAlw$_{cl}$ in PICA705. This effect results because biases of all-sky longwave radiation diagnostics and diagnostics of longwave cloud radiative forcings include additional errors due to the poorer sampling of cloudiness in the orbit simulations relative to that in the true simulation.

5.2. Zonal Mean Samplings

We now focus our discussion on the diurnal and spatial sampling biases computed over the 60-month simulations. Table 4 is as Table 3 but summarizes zonal mean sampling biases among PICA705, PICA485, and ICESAT, and the true simulation. In Table 4 the sampling bias is defined as the zonal mean difference between the satellite and the true diagnostics, between July 2001 and June 2006. Here the time-averaged bias contains information, not only on the impact of the diurnal sampling but also on the impact of the seasonal cycle of the sampling bias on the satellite diagnostics. Sigma is defined as the standard deviation of the zonal mean biases computed from the 60-month-averaged bias and is a measure of the amplitude of the seasonal cycle of the zonal mean sampling error. Unlike in section 5.1 where σ was defined as a spatial standard deviation, i.e., σ was computed from the global mean bias, σ is in this section computed from the 60-month time-averaged bias and is a temporal standard deviation.

Comparing Table 4 against Table 3 reveals that zonal mean longwave radiation diagnostics show similar patterns of diurnal and spatial sampling biases as regional diagnostics. As on regional scales, the bias of zonal mean net longwave radiation decreases between the surface and the top of the atmosphere, for both all-sky and clear-sky conditions. As for regional diagnostics, this effect results because of the decreased sensitivity of the top of the atmosphere relative to the surface net longwave radiation to the diurnal cycle of the land surface temper-

ature. As already seen in Table 3, σ values of all longwave radiation diagnostics increase between PICA705, and PICA485 and ICESAT, in response to the decreased number of accumulated coincident grid points and increased difference in the number of satellite overpasses between neighboring model grid points.

The latitude versus time cross sections of the zonally averaged $SFClw_{cl}$ simulated with the CSU GCM and zonally averaged bias in $SFClw_{cl}$ obtained with ICESAT, PICA485, and PICA705 are shown in Plate 3. The seasonal cycle of $SFClw_{cl}$ simulated with the CSU GCM is clearly seen in the top left panel of Plate 3. As already discussed in Figure 3, $SFClw_{cl}$ is minimum along the ITCZ, because of the downward longwave emission of water vapor. Along the equator the decrease in $SFClw_{cl}$ between July and January results because of the decrease in $SFClw_{cl}$ over the western Pacific and Indian Oceans, in conjunction with the seasonal shift of the monsoon flow simulated by the CSU GCM. Maxima in $SFClw_{cl}$ seen in the middle latitudes can be explained in terms of the strengthening of the storm track regions in the winter hemisphere. The increase in $SFClw_{cl}$ associated with the strengthening of the storm track regions over the Pacific and Atlantic Oceans explains the zonal mean maxima in $SFClw_{cl}$ observed between 30°N and 60°N in January. The zonal mean maxima in $SFClw_{cl}$ observed between 30°S and 60°S in July results because of the decrease in $SFClw_{cl}$ over the storm track regions in the Southern Hemisphere.

Plate 3 reveals that between 60°N and 30°S, PICA705 yields a systematic overestimate in the zonally averaged $SFClw_{cl}$ during the entire 60-month simulation, except along a narrow latitudinal band located south of the equator in winter. The magnitude of the zonal mean bias varies between zero and 2 W m^{-2} along the equator to values in excess of 4–10 W m^{-2} along the subtropics, the greatest bias occurring at 30°N. At 30°N this maximum zonal mean bias coincides with the positive regional bias observed over the Sahara desert and the Tibetan Plateau (refer to Figure 3). At 60°S the negative zonal mean bias results because of the negative regional mean bias seen over the Southern Oceans, as also seen in Figure 3. Because the number of coincident grid points between the PICASSO satellite and the EOS PM remains relatively constant during the 60 months of simulation, the latitude versus time pattern in the zonal mean bias in $SFClw_{cl}$ is similar from one month to the next at all latitudes. Between 30°N and 30°S the zonal mean bias in $SFClw_{cl}$ does not show a strong seasonal cycle over the 60-month simulation. In contrast to PICA705, month-to-month variations in the number of satellite overpasses yields a noisier pattern in the zonal mean bias of $SFClw_{cl}$ in PICA485. As for PICA705, the zonal mean bias is the largest at extratropical latitudes and the smallest at equatorial latitudes. As already discussed in section 5, the noisiness in the latitude versus time cross section of $SFClw_{cl}$ results because the number of coincident grid points between the PICASSO satellite flying at the altitude of 485 km varies from one month to the next. The 60-month zonal mean biases in $TOAlw_{cl}$ for PICA705 and PICA485 display very similar temporal distributions as $SFClw_{cl}$, but their magnitudes are reduced, as we would expect from Table 4. This map is omitted here for brevity.

6. Impact of Cloudiness

The chief goal in combining observations from the EOS-PM platform and the PICASSO and ICESAT satellites is to collect simultaneous measurements of the radiative and optical properties of clouds. The vertical distribution of cloudiness and how that distribution affects the top of the atmosphere, atmospheric, and surface energy budgets are of particular interest.

The spatial and temporal diurnal sampling impacts on the longwave radiative effect of clouds are best analyzed by looking at the bias and σ of the longwave cloud radiative forcing at the top of the atmosphere (TOAlwcrf), in the atmosphere (ATMlwcrf) and at the surface (SFClwcrf). TOAlwcrf and SFClwcrf are both positive and defined as the difference between the clear-sky and the all-sky net longwave radiation. Because the ATM net longwave radiation is negative (indicating a cooling of the atmosphere) and the absolute value of $ATMnetlw_{cl}$ is greater than that of ATMnetlw, we define ATMlwcrf as the difference between the all-sky and the clear-sky net longwave radiation so that it is a positive quantity, as TOAlwcrf and SFClwcrf. As defined above, TOAlwcrf, SFClwcrf, and ATMlwcrf represent a reduction in longwave cooling at the top of the atmosphere, at the surface, and in the atmosphere due to the presence of clouds. Regional mean biases in TOAlwcrf, SFClwcrf, and ATMlwcrf are mostly dependent on the diurnal variability of cloudiness since the diurnal sampling effect of the surface temperature is removed when subtracting the all-sky from the clear-sky net longwave radiation in the definition of the longwave cloud radiative forcing. The regional sampling error in SFClwcrf (TOAlwcrf and ATMlwcrf) is, of course, equal to the difference between the regional sampling errors in $SFClw_{cl}$ ($TOAlw_{cl}$ and $ATMlw_{cl}$) and SFClw (TOAlw and ATMlw). The effect of reduced diurnal samplings of the surface temperature and atmospheric temperature and water vapor are removed, leaving the reduced diurnal sampling of cloudiness to contribute a major part to the sampling bias in the longwave cloud radiative forcing. Table 3 reveals that in contrast to the biases and σ in the clear-sky and all-sky net longwave radiation, the absolute value of the biases and σ of the longwave cloud radiative forcing increases between the surface and the top of the atmosphere for the three simulations. In PICA705 the absolute values of the biases in SFClwcrf, ATMlwcrf, and TOAlwcrf are equal to 0.02, 0.28, and 0.30 W m^{-2}, respectively. As for the clear-sky and all-sky net longwave radiation, σ increases as the diurnal sampling decreases. At the top of atmosphere, σ is equal to 6.5 W m^{-2} in PICA705 while equal to 19.8 and 17.3 W m^{-2} in PICA485 and ICESAT, respectively. In the three simulations the bias and σ in TOAlwcrf and ATMlwcrf have the same magnitude, indicating that a decreased diurnal sampling of the cloudiness has a greater effect at the top of the atmosphere and in the atmosphere than at the surface.

Regional and zonal mean sampling errors of cloud diagnostics routinely output by the CSU GCM are gathered in Tables 5 and 6, respectively. Acronyms used in both tables are listed in Table 2. One of the most interesting feature to note is that in contrast to longwave radiation-related diagnostics, regional and zonal mean sampling errors do not increase as the number of accumulated coincident grid points decrease, but σ values do. For instance, the regional bias in Fclr is equal to 0.43% in PICA705 and equal to 1.36 and 0.23% in PICA485 and ICESAT, although the diurnal sampling is strongly reduced in PICA485 and ICESAT relative to PICA705. In contrast, the σ value of Fclr increases from 8.3 to 25.1% and 22.2% between the three simulations. Finally, the absolute value of the regional bias is the largest for the most abundant cloud type. In PICA705, absolute biases in Fwcld, Fmcld, and Ficld are equal

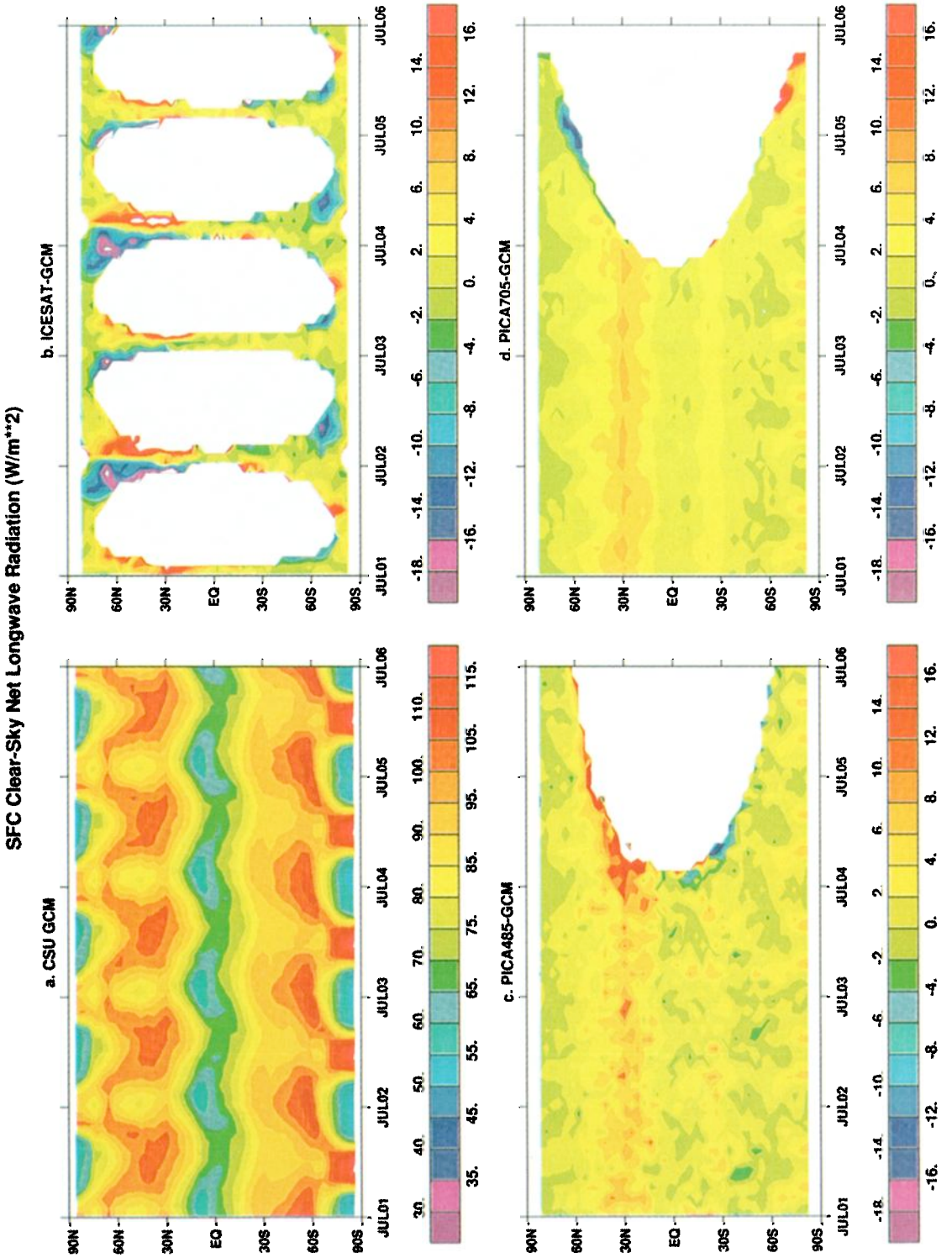

Plate 3. Latitude versus time cross sections of (a) the zonally averaged SFC clear-sky net longwave radiation ($SFClw_{cl}$) simulated with the CSU GCM, (b) the difference in $SFClw_{cl}$ between the ICESAT and the CSU GCM, (c) the difference in $SFClw_{cl}$ between the PICA485pm and the CSU GCM, and (d) the difference in $SFClw_{cl}$ between the PICA705pm and the CSU GCM.

Table 5. Regional Sampling Errors of Cloud-Related Diagnostics for July 2001

GCM Diagnostics	Units	PICA705		PICA485		ICESAT	
		Bias	σ	Bias	σ	Bias	σ
Fclr	%	0.43	8.33	1.36	25.11	0.23	22.19
Fcld	%	−0.43	8.33	−1.36	25.11	−0.23	22.19
Fwcld	%	−0.03	6.76	0.07	20.38	−0.18	18.60
Ficld	%	−0.51	10.20	−1.20	29.95	−0.35	27.53
Fmcld	%	−0.34	8.95	−0.07	27.24	0.24	24.41
Fovlp	%	−0.74	9.96	−0.26	29.63	−0.45	27.32
Foptd	per hPa	−0.10	2.70	−0.16	8.21	−0.12	7.85

to 0.03, 0.34, and 0.51%, while globally averaged amounts of Fwcld, Fmcld, and Ficld are equal to 14.2, 29.4, and 60.8%, respectively.

7. Summary and Conclusion

Means to measure the radiative and optical properties of multilayer cloud systems are to combine top-of-the-atmosphere radiative measurements from conventional passive scanning radiometers with measurements of the vertical distributions of clouds and their optical properties from lidars and radars in space. The disadvantage in using spatially and temporally collocated observations from two different spacecrafts is a poorer diurnal sampling of radiation and clouds relative to the one made by each satellite independently. The goal of this study was to estimate the magnitude of this diurnal sampling bias on top-of-the-atmosphere, atmospheric, and surface longwave radiative energy budgets and cloud properties by tracking the path of coincident grid points between the ICESAT and the PICASSO satellites and the EOS-PM platform using the CSU GCM.

1. The poorer sampling of the diurnal cycle of the surface temperature in ICESAT, PICA485, and PICA705 relative to that in the CSU GCM contributes a major part to the magnitude of the regional and zonal mean biases and σ. Because the effect of the diurnal cycle of the surface temperature peaks at the surface and decreases with height, regional and zonal mean biases and σ of the net longwave radiation at the surface are greater than those of the atmosphere and at the top of the atmosphere. Regional and zonal mean biases and σ of the longwave radiative heating rates are also greater in the lower than in the upper troposphere. This result applies to the three orbits under all-sky and clear-sky conditions.

2. In contrast to biases in the longwave net radiation budgets, biases and σ in the longwave cloud radiative forcings are the smallest at the surface and the largest at the top of the atmosphere. This makes sense because the contribution of decreased samplings of the surface temperature and atmospheric temperatures and water vapor have been removed, and regional and zonal mean biases can be explained in terms of the diurnal sampling of cloudiness only.

3. Biases and σ values of longwave radiation diagnostics increase as the number of coincident grid points between the EOS-PM Sun-synchronous orbit and the lower inclination orbit (PICA705, PICA485, and ICESAT) decreases. The factor of 8 decrease in the number of accumulated coincident grid points between PICA705 and PICA485 and ICESAT should theoretically leads to a 2.8 increase in the σ values between PICA705 and the other two satellite simulations. This agrees well with the results shown in Tables 3 and 5 for the longwave radiation and cloud-related diagnostics.

The magnitudes of the regional and zonal mean biases and σs listed in Tables 3–6 are, to a certain extent, dependent on the spatial resolution of the CSU GCM. We expect the impact of the GCM grid size to be greater in PICA485 and ICESAT than in PICA705 because the geographic distributions of the monthly averaged number of satellite overpasses are noisier in those two simulations. Increasing the spatial resolution of the CSU GCM would increase the spatial standard deviation of the mean biases of all radiative and cloud diagnostics. Increasing the horizontal resolution of the CSU GCM would also modify the simulated climate, enhancing regional differences in the geographical distributions of longwave radiation budgets and cloudiness. Therefore we would expect significant differences in the magnitude of the mean biases as well. To quantitatively determine the actual impact of increasing the spatial resolution of the CSU GCM would require to run new ICESAT, PICA485, and PICA705 simulations as future research.

Table 6. Zonal Mean Sampling Errors of Cloud-Related Diagnostics Between July 2001 and June 2006

GCM Diagnostics	Units	PICA705		PICA485		ICESAT	
		Bias	σ	Bias	σ	Bias	σ
Fclr	%	0.309	1.166	0.351	4.224	0.004	6.886
Fcld	%	−0.309	1.166	−0.351	4.224	−0.004	6.886
Fwcld	%	−0.140	0.970	0.008	3.701	0.055	5.373
Ficld	%	−0.287	1.407	−0.485	5.879	−0.146	8.899
Fmcld	%	−0.542	1.477	−0.478	4.892	−0.220	7.713
Fovlp	%	−0.492	1.432	−0.505	5.504	−0.163	8.655
Foptd	per hPa	−0.089	0.467	−0.045	1.484	0.093	2.871

Acknowledgments. This research was sponsored by the National Aeronautics and Space Administration under grant NAG-1-1266 to Colorado State University. Computing resources were provided by the National Center for Computational Sciences at NASA Goddard.

References

Arakawa, A., and W. H. Schubert, The interactions of a cumulus cloud ensemble with the large-scale environment, part I, *J. Atmos. Sci.*, *31*, 674–701, 1974.

Barkstrom, B. R., and G. L. Smith, The Earth Radiation Budget Experiment: Science and implementation, *J. Geophys. Res.*, *24*, 379–390, 1986.

Baum, B. A., D. P. Kratz, P. Yang, Y. X. Hu, P. F. Soulen, and S. C. Tsay, Remote sensing of cloud properties using MODIS airborne simulator imagery during SUCCESS, 1, Data and models, *J. Geophys. Res.*, *105*, 11,767–11,780, 2000a.

Baum, B. A., P. F. Soulen, K. I. Strabala, M. D. King, S. A. Ackerman, and W. P. Menzel, b., Remote sensing of cloud properties using MODIS airborne simulator imagery during SUCCESS, 2, Cloud thermodynamic phase, *J. Geophys. Res.*, *105*, 11,781–11,792, 2000b.

Charlock, T. P., F. Rose, T. Alberta, G. L. Smith, D. Rutan, N. Manalo-Smith, P. Minnis, and B. A. Wielicki, Cloud profiling radar requirements: Perspective from retrievals of the surface and atmosphere energetics. Utility and feasibility of a cloud profiling radar, in *Proceedings of the GEWEX Topical Workshop*, 46 pp., World Meteorol. Organ., Geneva, 1994.

Chou, M. D., Broadband water vapor transmission functions for atmospheric IR flux computations, *J. Atmos. Sci.*, *41*, 1775–1778, 1984.

Chou, M. D., and L. Peng, A parameterization of the absorption in the 15 μm CO_2 spectral region with application to climate sensitivity studies, *J. Atmos. Sci.*, *32*, 409–418, 1984.

Ding, P., and D. A. Randall, A cumulus parameterization with multiple cloud base levels, *J. Geophys. Res.*, *103*, 11,341–11,353, 1998.

Fowler, L. D., and D. A. Randall, Liquid and ice cloud microphysics in the CSU general circulation model, Part II, Impact on cloudiness, the Earth's radiation budget, and the general circulation of the atmosphere, *J. Clim.*, *9*, 530–560, 1996.

Fowler, L. D., and D. A., Randall, Simulation of upper tropospheric clouds with the Colorado State University general circulation model, *J. Geophys. Res.*, *104*, 6101–6121, 1999.

Fowler, L. D., D. A. Randall, and S. A. Rutledge, Liquid and Ice Cloud Microphysics in the CSU general circulation model, part I, Model description and simulated microphysical processes, *J. Clim.*, *9*, 489–529, 1996.

Geleyn, J.-F., and A. Hollingsworth, An economical analytical method for the computation of the interaction between scattering and line absorption of radiation, *Beitr. Phys. Atmos.*, *52*, 1–16, 1979.

Harshvardhan, R. Davies, D. A. Randall, and T. G. Corsetti, A fast radiation parameterization for atmospheric general circulation models, *J. Geophys. Res.*, *92*, 1009–1016, 1987.

Harshvardhan, D. A. Randall, T. G. Corsetti, and D. A. Dazlich, Earth radiation budget and cloudiness simulation with a general circulation model, *J. Atmos. Sci.*, *46*, 1922–1942, 1989.

Huffman, G. J., R. F. Adler, P. Arkin, A. Chang, R. Ferraro, A. Gruber, J. Janowiak, A. McNab, B. Rudolph, and U. Schneider, The Global Precipitation Climatology (GPCP) combined precipitation data set, *Bull. Am. Meteorol. Soc.*, *78*, 5–20, 1997.

Jakob, C., and S. A. Klein, The role of vertically varying cloud fraction in the parameterization of microphysical processes in the ECMWF model, *Q. J. R. Meteorol. Soc.*, *125*, 941–965, 1999.

Joseph, J. H., W. J. Wiscombe, and J. A. Weinman, The Delta-Eddington approximation for radiative flux transfer, *J. Atmos. Sci.*, *33*, 2452–2459, 1976.

King, M. D., Y. J. Kaufman, W. P. Menzel, and D. Tanre, Remote sensing of cloud, aerosol, and water vapor properties from MODIS, *IEEE Trans. Geosci. Remote Sens.*, *30*(1), 2–27, 1992.

Lacis, A. A., and J. E. Hansen, A parameterization for the absorption of solar radiation in the earth's atmosphere, *J. Atmos. Sci.*, *31*, 118–133, 1974.

Lin, Y.-L., R. D. Farley, and H. D. Orville, Bulk parameterization of the snow field in a cloud model, *J. Clim. Appl. Meteorol.*, *22*, 1065–1092, 1983.

Lord, S. J., Development and observational verification of a cumulus parameterization, 359 pp., Ph.D. dissertation, Univ. of Calif., Los Angeles, 1978.

McCormick, M. P., et al., Scientific investigations planned for the Lidar In Space Technology Experiment (LITE), *Bull. Am. Meteorol. Soc.*, *74*, 205–214, 1993.

Morcrette, J.-J., and Y. Fouquart, The overlapping of cloud layers in shortwave radiation parameterizations, J. Atmos. Sci., *43*, 321–328, 1986.

Pan, D.-M., and D. A. Randall, A cumulus parameterization with a prognostic closure, *Q. J. R. Meteorol. Soc.*, *124*, 949–981, 1998.

Roberts, R. E., J. E. A. Selby, and L. Biberman, Infrared continuum absorption by atmospheric water vapor in the 8–12 mm window, *Appl. Opt.*, *5*, 2085–2090, 1976.

Rodgers, C. D., Some extensions and applications of the new random model for molecular band transmission, *Q. J. R. Meteorol. Soc.*, *94*, 99–102, 1968.

Rossow, W. B., and R. A. Schiffer, Advances in understanding clouds from ISCCP, *Bull. Am. Meteorol. Soc.*, *80*, 2261–2287, 1999.

Rutledge, S. A., and P. V. Hobbs, The mesoscale and microscale structure and organization of clouds and precipitation in midlatitude cyclones, VIII, A model for the "seeder-feeder" process in warm-frontal rainbands, *J. Atmos. Sci.*, *40*, 1185–1206, 1983.

Schiffer, R. A., and W. B. Rossow, The International Satellite Cloud Climatology Project (ISCCP): The first project of the World Climate Research Program, *Bull. Am. Meteorol. Soc.*, *64*, 779–784, 1983.

Simpson, J., R. A. Adler, and G. R. North, A proposed Tropical Rainfall Measuring Mission (TRMM) satellite, *Bull. Am. Meteorol. Soc.*, *69*, 275–295, 1988.

Stephens, G. L., Radiation profiles in extended water clouds, part II, Parameterization schemes, *J. Atmos. Sci.*, *35*, 2123–2132, 1978.

Stephens, G. L., Future satellite observations of clouds, in *Cloud Processes and Cloud Feedbacks in Large-Scale Models, GCSS-WGNE Workshop*, 9–13 November, Eur. Cent. for Medium-Range Weather Forecasts, Reading, England, 1998.

Suarez, M. J., A. Arakawa, and D. A. Randall, Parameterization of the planetary boundary layer in the UCLA general circulation model: Formulation and results, *Mon. Weather Rev.*, *111*, 2224–2243, 1983.

Tian, L., and J. A. Curry, Cloud overlap statistics, *J. Geophys. Res.*, *94*, 9925–9935, 1989.

Young, D. F., P. Minnis, D. R. Doelling, G. G. Gibson, and T. Wong, Temporal interpolation methods for the Clouds and the Earth's Radiant Energy System (CERES) experiment, *J. Appl. Meteorol.*, *37*, 572–590, 1998.

Wang, J. W., and W. B. Rossow, Determination of cloud vertical structure from upper-air observations, *J. Appl. Meteorol.*, *34*, 2243–2258, 1995.

Warren, S. G., C. J. Hahn, and J. London, Simultaneous occurrence of different cloud types, *J. Clim. Appl. Meteorol.*, *24*, 658–667, 1985.

Wielicki, B. A., R. D. Cess, M. D. King, D. A. Randall, and E. F. Harrison, Mission to planet earth: Role of clouds and radiation in climate, *Bull. Am. Meteorol. Soc.*, *76*, 2125–2153, 1995.

Wielicki, B. A., B. R. Barkstrom, E. F. Harrison, R. B. Lee III, G. L. Smith, and J. E. Cooper, Clouds and the earth's radiant energy system, *Bull. Am. Meteorol. Soc.*, *77*, 853–868, 1996.

Winkes, D. A., and B. A. Wielicki, The PICASSO-CENA Mission, in *Sensors, Systems, and Next Generation Satellites*, edited by H. Fujisada, *Proc. SPIE*, *3870*, 2000.

M. D. Branson, D. Fowler, and D. A. Randall, Department of Atmospheric Science, Colorado State University, Fort Collins, CO 80523. (laura@slikrock.atmos.colostate.edu)

G. G. Gibson and B. A. Wielicki, Atmospheric Science Division, NASA Langley Research Center, Hampton, VA 23681.

F. M. Denn, Analytical Services & Materials Inc., One Enterprise Parkway, Suite 300, Hampton, VA 23666-5845.

(Received September 29, 1999; revised February 17, 2000; accepted March 25, 2000.)